THE JOURNAL OF PHYSICAL CHEMISTRY C

Article

Cite This: J. Phys. Chem. C 2018, 122, 18596−18602

pubs.acs.org/JPCC

Direct Evidence of Surface Charges in n-Type Al-Doped ZnO

Dongming Zhou,[†,§] Peijian Wang,[‡] Christopher R. Roy,[†] Michael D. Barnes,*[,†,‡] and Kevin R. Kittilstved*[,†]

[†]Department of Chemistry and [‡]Department of Physics, University of Massachusetts Amherst, Amherst, Massachusetts 01003, United States

Supporting Information

ABSTRACT: The fundamental properties of electrons in the prototypical n-type oxide nanocrystal, Al^{3+}-doped ZnO, have been studied at both the ensemble and single-particle levels by spectroscopic and electron force microscopic techniques. We developed and implemented a new synthetic methodology that enables the tunable incorporation of Al^{3+} in the ZnO nanocrystal in an "etching−regrowth−doping" (ERD) strategy in a single-pot reaction. The ensemble-averaged properties and evolution of the Al^{3+} speciation in ZnO were studied using electronic absorption spectroscopy and powder X-ray diffraction and reveal the successful substitution of Al^{3+} only after implementation of the ERD strategy. Characterization of individual ZnO, surface Al^{3+}-doped ZnO, and internal Al^{3+}-doped ZnO nanocrystals using electrostatic force microscopy reveals strong responses in both the quantity of surface charges and electron polarizabilities, which are dependent on the amount of Al^{3+} in the ZnO lattice. These results appear to suggest that an upper limit to the electron polarizability exists for Al^{3+}-doped ZnO nanocrystals.

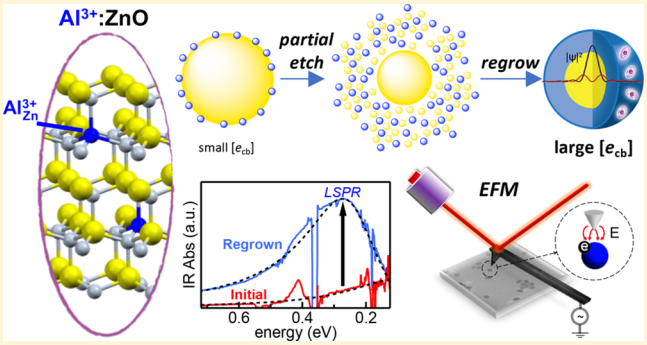

INTRODUCTION

Aliovalent-doped semiconductor nanocrystals (NCs) are anticipated to have broad new optoelectronic applications that derive from increased carrier concentrations relative to their bulk analogues. In colloidal metal oxide NCs such as ZnO and In_2O_3, the stabilization of high conduction band electron (e_{cb}) densities of 10^1 to 10^2 e_{cb} per NC has been demonstrated through aliovalent doping with donors such as Al^{3+} in ZnO (AZO) and Sn^{4+} in In_2O_3 (indium tin oxide).[1,2] These high e_{cb} densities lead to interesting physical properties including tunable surface plasmon resonances in the near-infrared (IR) to mid-IR regions, which could be utilized in electrochromic smart windows to control heat flow in buildings by reflecting or transmitting IR radiation. Recently, both n- and p-type plasmonic NCs have revealed large cyclotron resonances suggesting significant orbital contributions, which open the door to potential plasmon−exciton technologies.[3,4] However, carrier concentrations in n-type colloidal NCs, such as AZO, typically account for only a small fraction of the overall concentration of aliovalent dopants in the NC. The seeming lack of control over dopant speciation and the unique defect chemistries to the NC are suspected to play significant roles in diminishing the n-type character in these promising optoelectronic materials. We demonstrate a new synthetic strategy for controlling the concentration and speciation of heterovalent dopants in ZnO NCs, yielding tunable carrier densities. The characteristics of these heavily-doped AZO NCs are probed by electrostatic force microscopy (EFM) on the single particle level.

Typical synthetic strategies for the preparation of air-stable n-type colloidal semiconductor NCs incorporate aliovalent dopants directly during the crystal growth.[5−9] Although recent synthetic advances have demonstrated better control over the growth kinetics of pure NCs, there is typically still lack of reproducible control over the yield of dopant incorporation in doped NC syntheses.[9] Hutchison and co-workers recently developed a new synthesis strategy that relies on intricate control over the NC growth kinetics by restricting the rate at which metal oleate precursors are reacted with long-chain alcohol solutions at high temperatures.[7,8] This strategy has proven successful in producing n-type oxide NCs that display localized surface plasmon resonances (LSPRs).[7,9] Despite the potential of these doped NCs as tunable IR absorbing materials, only a small percentage of the aliovalent dopants are responsible for these exotic phenomena. The percentage of "active" dopants is very sensitive to the specific reaction conditions and thus contribute to wide batch-to-batch variations in the NC composition and morphology and activity of Al^{3+} dopants in ZnO NCs. In this report, we utilize a single-pot approach and allow rapid nucleation and growth kinetics to dictate the formation of a core/shell NC that has an undoped ZnO core with dopants residing on the NC surface. Subsequent incorporation of dopant ions is initiated by the addition of controlled amounts of oleic acid (OA) at lower

Received: May 17, 2018
Revised: July 17, 2018
Published: July 19, 2018

DOI: 10.1021/acs.jpcc.8b04718
J. Phys. Chem. C 2018, 122, 18596−18602

temperature to etch the NC surface, resulting in a smaller undoped ZnO core ("seed") and free Zn- and Al-oleate precursors in solution. Lower growth temperatures and higher relative concentrations of $Al(oleate)_3$ compared to $Zn(oleate)_2$ enable competitive kinetics during growth to allow for tunable and reproducible dopant incorporation during NC regrowth. This etching and regrowth strategy routinely produces dopant activation of the highest percentages of active Al^{3+} dopants in AZO NCs reported to date.

Direct measurement of surface localized electronic states or trap sites remains elusive, but has been implicated to explain luminescence dynamics including blinking in numerous NC systems.[10,11] EFM is a very sensitive technique for studying localized charges (q) of single nanoparticles and has been utilized to quantify the charges on NC surfaces, including CdSe quantum dots (QDs) under ambient conditions (q < 1 e),[12,13] laser excitation of the excitonic transition under N_2 gas ($q \approx 1-2$ e),[14] and electrical bias on conductive substrates (q < 7 e).[15] It has also revealed the existence of interfacial charge separation upon illumination of plasmonic Au−CdSe nanorod hybrids (CdSe q < 7 e).[16] The investigation of surface charges in n-type metal oxides and chalcogenides by EFM has been applied here to investigate the surfaces of large Al^{3+}-doped ZnO (AZO) NCs with varying concentrations of delocalized carriers estimated from fitting the LSPR band by a modified Drude model.

Here, we describe the synthesis and structural electronic characterization of AZO-doped NCs with tunable e_{cb} densities using an etching−regrowth−doping (ERD) synthetic strategy. Surface versus core Al^{3+} speciation in the AZO NCs is shown to be easily tuned by this new etching and regrowth synthetic procedure revealed by X-ray scattering that suggests a positive correlation between dopant speciation and dopant activation. Fourier transform infrared (FTIR) measurements revealed strong and tunable infrared surface plasmon resonances indicating the presence of mobile carriers. These ensemble measurements are comparable to EFM measurements on individual AZO NCs that exhibit a large number of surface charges (q > 100 e in highly active plasmonic AZO NCs). Other batches of AZO NCs exhibiting weaker LSPR exhibit a significant decrease in the surface charges (q = ∼20−45 e), but not as low as pure ZnO NCs (q = 0). We also calculate experimental electron polarizabilities that are roughly 2 orders of magnitude larger in the AZO NCs compared to undoped ZnO NCs. These results provide new insight into the possible origin of electron stability in these degenerately doped NCs.

EXPERIMENTAL SECTION

Materials. All chemicals were used without additional purification. Sodium hydroxide (NaOH 98.9%) was purchased from Fisher; zinc chloride ($ZnCl_2$, 97%) and OA (technical grade, 90%) were purchased from Alfa Aesar; 1-dodecanol (DDOH, 98%) and 1-octadecene (ODE, technical grade 90%) were purchased from Acros Organics; and aluminum chloride ($AlCl_3$ anhydrous, 99%) was purchased from Strem Chemicals.

Synthesis of Zinc and Aluminum Oleates. The oleate complexes of zinc and aluminum were synthesized following literature methods.[17] In brief, 20 mmol anhydrous zinc or aluminum chloride was dissolved in 100 mL of methanol, followed by addition of OA (2 equiv for Zn; 3 equiv for Al). After all precursors were dissolved, 200 mL of a methanolic solution of NaOH (60 mmol for aluminum oleate and 40 mmol for zinc oleate) was added dropwise into the metal precursor solution. The product zinc or aluminum oleate immediately precipitated out of solution and was washed four to five times with methanol before drying under vacuum overnight. We attempted the synthesis of metal oleates using hydrated metal chloride salts or tetramethylammonium hydroxide pentahydrate as the base,[18] however, these hydrated precursors produced negative results compared to the anhydrous precursors for Al^{3+}-doping of ZnO.

Synthesis of AZO NCs Using the ERD Method. In a typical reaction for AZO NCs, $Zn(oleate)_2$ (0.63 g, 1 mmol) and $Al(oleate)_3$ (0.17 g, 0.2 mmol) were dissolved in a 50 mL three-necked flask containing 10 mL of ODE. The solution was heated to 100 °C under vacuum for 10 min to remove any adventitious water. The solution was then heated to 300 °C under an argon flow. A separate solution of 10 mmol DDOH in 2 mL of ODE was heated to 150 °C and rapidly injected into the reaction flask at 300 °C. The reaction temperature dropped to 280 °C, and the solution was kept at this temperature for 30 min to allow the ZnO precursor NCs to nucleate and grow. To initiate NC etching and regrowth, a solution of 2 mmol OA in 2 mL of ODE was heated to 150 °C and rapidly injected into the reaction solution followed by heating at 280 °C for another 40 min. The NCs were cooled to room temperature, washed three times with ethanol, and suspended in hexane for spectroscopic investigation.

Physical Methods. Electronic absorption spectra in the ultraviolet−visible region were collected on hexane suspensions with a Varian Cary 50 Bio spectrometer. FTIR spectra were collected on a Varian 670 FT spectrometer. Hexane suspensions were collected either in 1 cm path length quartz cuvettes or a 0.005 cm path length demountable cell (PIKE Industries) with KBr windows. Powder X-ray diffraction (PXRD) patterns were collected on precipitated powders using a PANalytical X'Pert Material Research Diffractometer. Microstructure calculations were performed using the MAUD computer program.[19] Transmission electron microscopy (TEM) images were collected on carbon-coated (3 nm) Cu TEM grids on a JEOL JEM 2000FX microscope. Particle size distributions from TEM images were performed using ImageJ.

EFM Measurements and Data Analysis. We carried out the EFM measurements on an Asylum Research MFP-3D atomic force microscope with Pt-coated probes (APPNano ANSCM-PA tips). The colloidal ZnO or AZO NCs were deposited on glass or highly oriented pyrolytic graphite (HOPG) substrates. We employed a multipass scan technique in which the initial scan measures the surface topography [atomic force microscopy (AFM)], and then the induced phase shift of the cantilever was measured as a function of the tip-substrate bias (EFM). The lift height during the EFM scans was fixed at 40 nm.[20−22]

The experimental phase response is composed of electric field and capacitive interactions, described by the linear combination of linear and quadratic terms: $\Delta\Phi = A \cdot V_{EFM} + B \cdot (V_{EFM})^2$, where A and B are fitting parameters related to charge and polarizability (α), respectively, as $A = q(\Omega/(kz^2))$ and $B = -3\alpha(\Omega/(kz^4))$.[15] Here, Ω is the quality factor, k is the spring constant (50 N/m), and z is the lift height.

RESULTS AND DISCUSSION

ERD Synthesis, Morphology, and Spectroscopy. Figure 1a summarizes our synthetic strategy to prepare AZO NCs involving a single-pot, multistep reaction. The nucleation of "initial" AZO NCs is initiated by the addition of oleyl

DOI: 10.1021/acs.jpcc.8b04718
J. Phys. Chem. C 2018, 122, 18596−18602

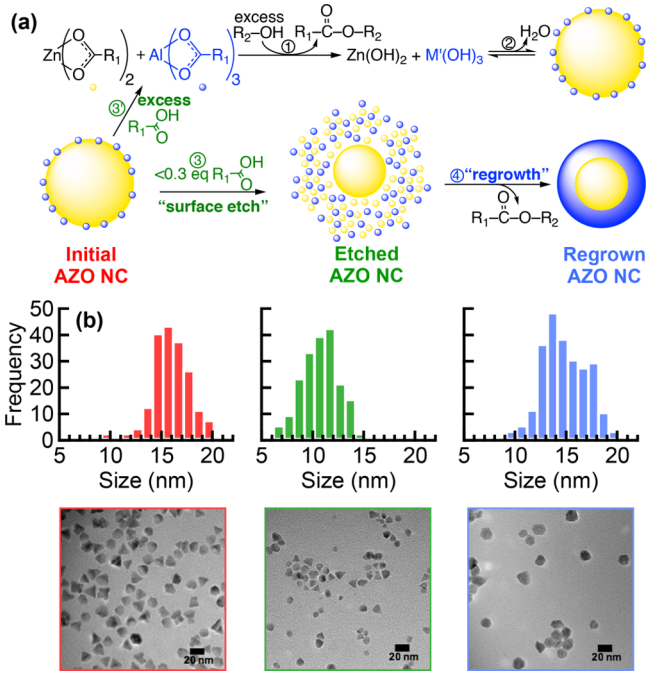

Figure 1. (a) Reaction scheme describing the ERD methodology for preparing tunable AZO NCs. (b) Particle size histograms (top) and TEM images (bottom) collected on aliquots of the initial AZO NCs (left), after adding OA to yield etch AZO NCs (middle), and then after allowing for the AZO NCs to regrow (right).

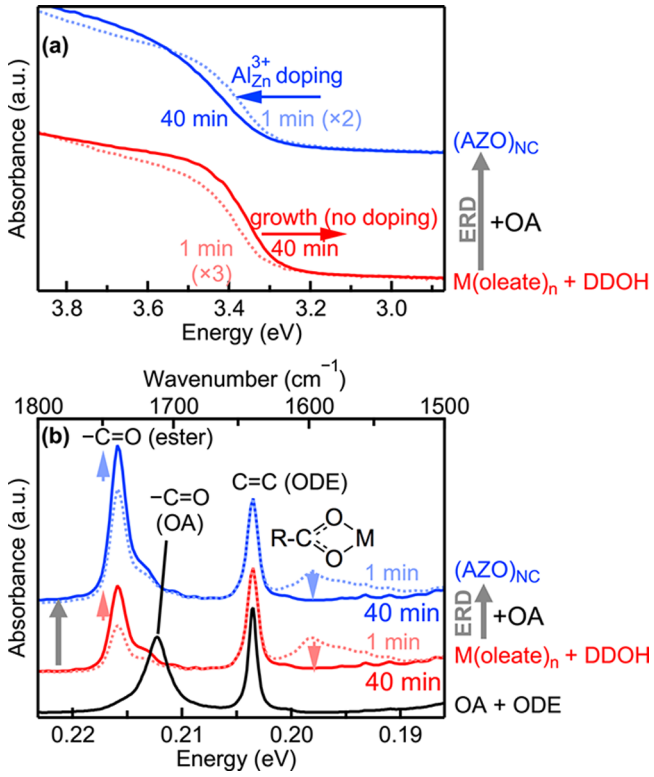

Figure 2. (a) Electronic absorption and (b) FTIR spectra of AZO NCs after the addition of DDOHto the initial oleate precursor solution at 300 °C (1 min = dashed red line; 40 min = solid red line) and after etching with 0.2 mmol OA (dashed blue line at 1 min) at 280 °C and allowing to regrow for 40 min (solid blue line). The FTIR spectrum of OA in ODE is included (black line). The spectra are normalized to the C═C stretch of the reaction solvent, ODE.

alcohol to a solution of Zn and Al oleate precursors in octadecene at 300 °C. TEM images shown in Figure 1b of the initial AZO NCs after growth at 280 °C for 40 min (step 2) display highly faceted NCs with an average diameter d = 15.3 ± 1.5 nm. After allowing the growth, but prior to NC purification, a substoichiometric amount of OA is added at a slightly lower temperature of 280 °C to *partially* etch the NCs (step 3). Successful etching of the initial AZO NC is confirmed by a decrease in the average NC diameter to 10.1 ± 1.6 nm, by TEM, collected on an aliquot 1 min after addition of OA. The partial etching step reintroduces both metal oleates into the growth solution albeit with a much higher Al/Zn ratio than in the initial reaction solution. Regrowth of the NCs for ∼40 min yields NCs of ∼14.0 ± 1.8 nm (step 3), which is comparable to the initial AZO NCs.

Peng and co-workers previously reported the shape evolution of the undoped ZnO NCs at different stages during a similar etching and regrowth method with OA substituted by stearic acid.[23] The initial AZO NCs shown in Figure 1b are consistent with a pyramidal shape. Thus, depending on the orientation of the pyramidal precursor AZO NCs on the TEM grid, the projection of the TEM images could appear triangular or hexagonal. After adding 2 mmol OA to the precursors for 1 min, smaller pseudospherical NCs appear. After 40 min of regrowth, the NCs become more irregular in shape. The change in the NC morphology observed during the etching and regrowth is likely caused by faster etching by OA at the apex of the nanopyramid compared to the sides and base.

The same aliquots taken during the reaction for TEM investigation were also studied by electronic absorption and FTIR spectroscopy to provide insight into the reaction progress by placing samples between KBr windows in a demountable IR cell holder with a 5 μm path length. The TEM images shown in Figure 1b reveal that the average sizes of the initial and regrown AZO NCs are both much larger than the excitonic Bohr radius of bulk ZnO, a_B = 2.34 nm.[24] Despite the presence of 20% (mol) Al(oleate)$_3$ in the reaction solution, the energy of the first exciton immediately after nucleation (∼1 min) and growth (40 min) red shifts to lower energies similar to bulk or undoped large ZnO NCs at ∼3.2 eV (see Figure 2a). The red shift is associated with ZnO growth and a low [e_{cb}]. On the basis of this observation, we depict these initial AZO NCs in Figure 1a as undoped ZnO NCs with Al residing only on the NC surface.

In contrast to the behavior of the initial AZO NCs, the electronic absorption spectra of the regrown AZO NCs display a significant blue shift of the ZnO band edge by ∼0.10 eV after etching with 2 mmol OA and allowing the AZO NCs to regrow for 40 min at 280 °C. This blue shift in the band edge energy indicates that the regrown AZO NCs possess a significant increase in the concentration of active Al^{3+} dopants and [e_{cb}]. The amount of OA added to etch the initial particles is critical to tuning the band edge and [e_{cb}] in the resulting AZO NCs, as shown in Figure S1. Addition of excess OA results in total dissolution of the ZnO core, and the AZO NCs that result from re-nucleation show a decreased [e_{cb}].

The reaction progress was followed by IR spectroscopy, as shown in Figure 2b. The driving force behind the nucleation and growth of ZnO NCs is the esterification reaction[25,26] between the metal oleate (M–O_2C–R_1) and DDOH (R_2–OH). The relevant reactants and products as well as their IR frequencies between 1500 and 1800 cm^{-1} are given in Table 1.

DOI: 10.1021/acs.jpcc.8b04718
J. Phys. Chem. C 2018, 122, 18596−18602

Table 1. Spectral Assignment of FTIR Stretches Observed in the Synthesis of AZO NCs by the ERD Method

assignment	molecule	$\hbar\omega$ (cm^{-1})	bandshape
ν_a(R−COO)	M(oleate)$_n$	1597	broad
ν(−C═C−)	octadecene	1641	narrow
ν(R−C═O)	OA	1712	narrow
ν(C═O, ester)	OA lauryl ester	1741	narrow

The IR spectra of OA in the solvent (ODE) is also included for reference. The IR spectra shown in Figure 2b are normalized to the intensity of the C═C stretch of ODE at 1641 cm^{-1}. The initial products after nucleation of the initial AZO NCs are detected by the broad metal oleate stretch at 1597 cm^{-1} and OA lauryl ester at 1741 cm^{-1}. After the initial growth step, the metal oleate stretch disappears and the ester peak increases in absorption. After addition of OA, the same features are observed: initial increase in the metal oleate concentration followed by a decrease in the metal oleate and increase in the ester absorption after regrowth. The reaction mechanism is the same, however, the amount of Al^{3+} incorporation is apparently very different before and after partial etching and regrowth.

LSPR Analysis. The electronic absorption spectra of the initial and regrown AZO NCs are shown in Figure 3a. In addition to the blue shift of the ZnO band gap that was presented in Figure 2a, there is also a significant change in the LSPR intensity and central position, as shown in Figure 3a. The initial AZO NC displays a very weak LSPR that extends below ~0.15 eV, suggesting a low percentage of active Al^{3+} dopants in these initial AZO NCs. The regrown AZO NCs, however, display a prominent LSPR at ~0.27 eV.

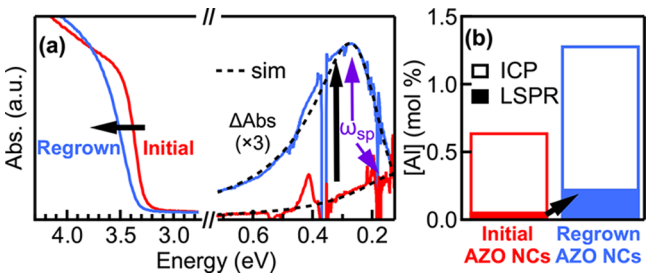

Figure 3. (a) Band gap absorption and LSPR for weakly activated AZO NCs (initial) and highly activated AZO (regrown) after the addition of OA to initiate ERD. (b) Analytical Al mol fraction (%) from ICP-AES (empty boxes) from nominally 20 Al mol % added to the reaction before and after ERD. The amount of "active" Al^{3+} in the different AZO NCs is estimated from the fitting of the LSPR line shape function using the modified Drude model (shaded region).

Estimates of the carrier concentration from the spectra shown in Figure 3a were obtained by fitting the LSPR to a modified Drude model[27−29]

$$\varepsilon(\omega) = \varepsilon_\infty - \frac{\omega_p^{\,2}}{\omega^2 + i\omega\Gamma(\omega)} \quad (1)$$

where ε_∞ is the high-frequency dielectric constant (ε_∞ = 3.71 for ZnO), ω_p is the bulk plasma frequency defined by the energy of the LSPR, and Γ is the frequency-dependent damping function that defines the line width of the LSPR. The carrier concentration (n) is extracted from the ω term that is equal to $(ne^2/(m^*\varepsilon_0))^{1/2}$, where e is the elementary charge, m^* is the carrier effective mass [$m^*(e_{cb})$ = 0.24m_e for ZnO and m_e is the electron mass], and ε_0 is the permittivity of free space.[28] Fitting of the LSPRs for the initial and regrown AZO NCs with eq 1 yields an average carrier concentration for the ensemble of $n = 2.1 \times 10^{19}$ cm^{-3} (~40 e_{cb}/NC) and 9.8×10^{19} cm^{-3} (~140 e_{cb}/NC), respectively. However, the lack of a clear peak maximum limits the reliability of these data and suggests an overestimation of the actual carrier concentration for the initial AZO NCs. The Al and Zn concentrations for both initial and regrown AZO NCs were determined analytically by inductively coupled plasma atomic emission spectroscopy (ICP-AES) measurements, and the Al mole fraction is shown in Figure 3b. The Al mole fraction for the regrown AZO NCs reaches 1.3% compared to just 0.6% Al in the initial AZO NC. On the basis of the analysis of the LSPR energy, we estimate that the percentage of active Al^{3+} ions increases from ~8% in the initial AZO NCs to ~18% for the regrown AZO NCs. In comparison to other reported AZO NCs with similar carrier concentrations and sizes, our AZO NCs prepared using the ERD strategy have ~2.5 times higher percentage of active Al^{3+} dopants.[5]

The ~500% increase in the average carrier concentration of the AZO NCs after etching and regrowth suggests an increase in hybridization between the Al^{3+} defects and the ZnO band structure. It is generally acknowledged that substitutional dopants in semiconductor NCs have superior electronic coupling to the host compared to surface-bound dopants.[30,31] Both isovalent and aliovalent transition metal dopants such as Co^{2+} and Fe^{3+} have been shown using spectroscopic techniques to substitute not only at Zn^{2+} lattice sites but also on the surface in pseudo-octahedral coordination of ZnO NCs.[32,33] Whereas Al^{3+} could occupy similar sites in the ZnO NC, there are few direct physical methods to determine the speciation of Al^{3+} because it is diamagnetic.

Structural Analysis. As an alternative to direct spectroscopic evidence of the Al^{3+} speciation in the AZO NCs, we performed a structural investigation via Rietveld refinement of the PXRD patterns as an indirect probe (see Figure 4a). The

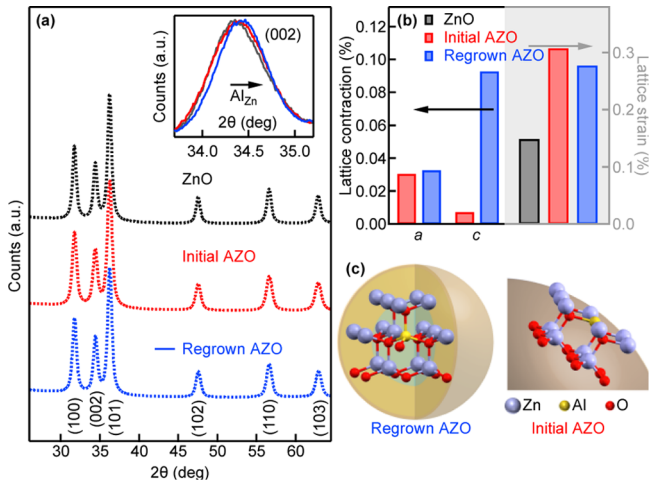

Figure 4. (a,b) PXRD data and Rietveld analysis of pure ZnO, less-activated AZO, and highly activated AZO NCs. The percent lattice contraction in panel (b) is relative to the undoped ZnO NCs prepared by the same method before etching. Lattice strain for undoped ZnO NCs is included for reference. (c,d) Local dopant structure illustration for two different AZO NCs. For highly activated AZO, the contribution to lattice contraction is due to the increased concentration of substitutional Al^{3+}, which has a smaller crystal radius compared to Zn^{2+} ions.

DOI: 10.1021/acs.jpcc.8b04718
J. Phys. Chem. C 2018, 122, 18596−18602

patterns for pure ZnO and the initial and regrown AZO NCs are nearly identical and only index to zincite.[34] The crystallite sizes estimated from the Scherrer equation for all AZO and pure ZnO NCs are similar to the observations from TEM (12−15 nm, see the Supporting Information). However, close inspection of the patterns reveals slight shifts of the reflections to larger 2θ with increasing total Al content in the AZO NCs, especially in the (002) peak. This effective lattice contraction is most pronounced in the c lattice parameter, as shown in Figure 4b, and is consistent with the substitution of smaller Al^{3+} ions (crystal radius, r_c = 0.53 Å) at Zn^{2+} sites (r_c = 0.74 Å).[35]

Microstructure analysis shown in Figure 4b (right axis) provides relative estimates of the lattice strain caused by point defects (extrinsic and intrinsic defects including vacancies) and size of a NC.[19] The undoped ZnO NCs provide a baseline for the expected lattice strain originating from the NC size. Strain analysis of both sets of AZO NCs display about twice the lattice strain that is attributed to changes in the microenvironments around the Al^{3+} defects. Thus, the increased strain for the AZO versus undoped ZnO is expected and similar to previous observations.[5] However, if the strain is considered among the two AZO NCs (initial vs regrown) on a per dopant basis, then the regrown AZO NCs would have a significantly lower amount of strain per Al^{3+} because the Al^{3+} content is 2 times larger than the less active initial AZO NC, as determined by ICP above. The lower strain per Al^{3+} for the regrown AZO NCs prepared by the ERD method suggest that more Al^{3+} defects occupy substitutional sites, which is consistent with the increased carrier concentration, as shown in Figure 3. Furthermore, the increased Al^{3+} incorporation is attributed to the lower regrowth temperature and increased $Al(oleate)_3$/$Zn(oleate)_2$ ratio after partial etching of the initial AZO NCs with OA.

EFM of Individual NCs. Figure 5 shows the phase-shift versus tip bias for representative pure ZnO and AZO NCs deposited on different substrates—glass and HOPG. The insets depict the corresponding surface morphologies and height line sections obtained from AFM measurements on individual NCs. In Figure 5a, the undoped NC on glass possesses a linear component with q = 0. By contrast, an AZO NC on glass shown in Figure 5b displays parabolic phase-shift behavior with a much higher slope of the linear component that indicates q = 91 e. The response of the AZO NCs deposited on conductive substrates such as HOPG is dominated by the linear component, as shown in Figure 5d. The calculated charge q = 124 e is of the same order of magnitude of that on glass. The pure ZnO NCs on HOPG shown in Figure 5c consistently displays a very small parabolic phase shift again with q = 0.

Figure 6 compares the electron polarizability term extracted from the fits for the EFM response for a statistically relevant number of pure ZnO NCs and initial and regrown AZO NCs deposited on glass versus q. The inset is a bar chart of the conduction band electrons estimated from the LSPR given in Figure 3a. The regrown AZO NCs possess polarizabilities that are 1−2 orders of magnitude greater than those of pure ZnO NCs, which is similar to previously reported values for pure CdSe NCs.[15] On the other hand, the initial AZO NCs have only a slightly smaller polarizability than the regrown AZO NCs. The polarizability directly links the dielectric constants (rather than the e_{cb}), which are closer for nonactivated and activated AZO NCs than the undoped ZnO NCs. We also measured gold nanoparticles as a reference (see Figure S3); the

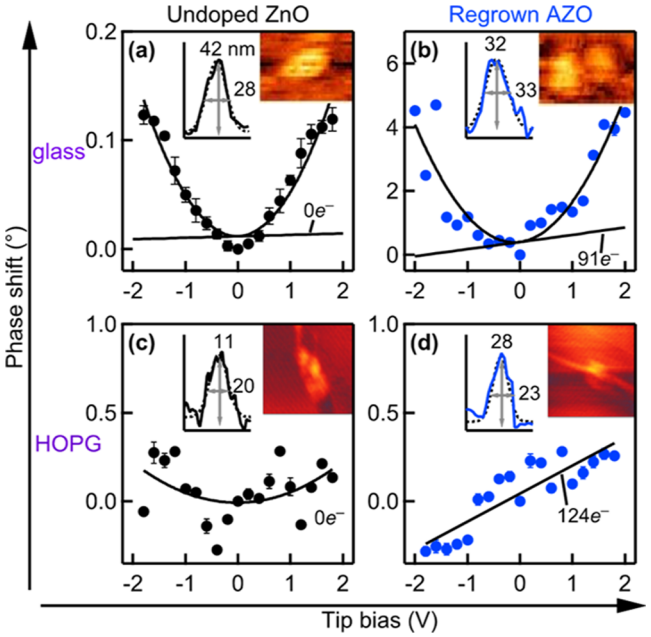

Figure 5. Representative phase shifts vs tip bias for different QDs: (a) undoped NC on glass, (b) activated-doped NC on glass, (c) undoped NC on HOPG, and (d) activated-doped NC on HOPG. The top-right inset shows representative AFM images for each sample. The insets show the amplitude and width line scans on individual NCs that were fit to a Gaussian profile. The phase shift data have been multiplied by −1 for stylistic purposes only.

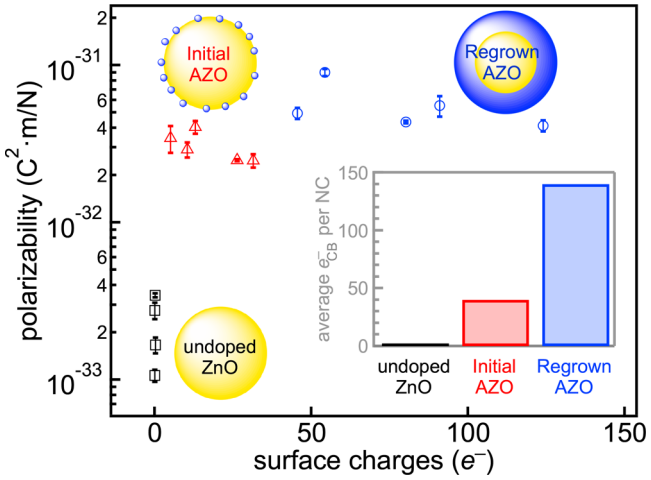

Figure 6. Polarizability vs surface charge scatter plot comparing undoped ZnO, weak LSPR AZO NCs, and strong LSPR AZO NCs deposited on glass. The inset is the ensemble averaged free carriers per NC for the different ZnO and AZO NCs determined by fitting the LSPR band to the Drude model.

gold nanoparticle has a surface charge close to zero (q = ∼1 e) and a polarizability that is ∼1−2 orders of magnitude higher than the average value of the regrown AZO NCs.[36,37] The average 140 e_{cb}/NC for the regrown AZO NCs combined with relative low polarizabilities confirms the localized surface charge measured by EFM. Despite the differences in q of the different AZO NCs, the polarizability of the charges associated with these AZO NCs are similar and on average is an order of magnitude larger than undoped ZnO NCs.

DOI: 10.1021/acs.jpcc.8b04718
J. Phys. Chem. C 2018, 122, 18596−18602

CONCLUSIONS

We have shown that an effective "single-pot" strategy based on ERD yields high-quality AZO NCs with a significantly enhanced number density and surface charge, as demonstrated by ensemble and single-particle measurements. By controlling the dopant speciation via low-temperature growth from seeded ZnO NCs using chemical etchants that also passivate the surface, we have demonstrated a new paradigm in inorganic electronic materials in which quantitative surface charge and polarizability can be detected and quantified directly using single-particle EFM measurements. This work further provides a clear distinction in the evolution of the structure and electronic characteristics of AZO NCs from nondoped to degenerately-doped.

ASSOCIATED CONTENT

Supporting Information

The Supporting Information is available free of charge on the ACS Publications website at DOI: 10.1021/acs.jpcc.8b04718.

Additional experimental methods, synthetic details, and characterization (PDF)

AUTHOR INFORMATION

Corresponding Authors

*E-mail: mdbarnes@chem.umass.edu (M.D.B.).
*E-mail: kittilstved@chem.umass.edu (K.R.K.).

ORCID

Michael D. Barnes: 0000-0002-6201-7284
Kevin R. Kittilstved: 0000-0002-9852-7454

Present Address

§Department of Chemistry, Zhejiang University, Hangzhou, Zhejiang, China.

Author Contributions

The manuscript was written through contributions of all authors. D.Z. and P.W. contributed equally.

Notes

The authors declare no competing financial interest.

ACKNOWLEDGMENTS

This work was partially supported by the National Science Foundation (CHE-1454930 to K.R.K.). C.R.R. was supported through the National Science Foundation REU program (CHE-1263075).

REFERENCES

(1) Schimpf, A. M.; Thakkar, N.; Gunthardt, C. E.; Masiello, D. J.; Gamelin, D. R. Charge-tunable quantum plasmons in colloidal semiconductor nanocrystals. *ACS Nano* **2014**, *8*, 1065−1072.

(2) Schimpf, A. M.; Knowles, K. E.; Carroll, G. M.; Gamelin, D. R. Electronic doping and redox-potential tuning in colloidal semiconductor nanocrystals. *Acc. Chem. Res.* **2015**, *48*, 1929−1937.

(3) Yin, P.; Tan, Y.; Fang, H.; Hegde, M.; Radovanovic, P. V. Plasmon-induced carrier polarization in semiconductor nanocrystals. *Nat. Nanotechnol.* **2018**, *13*, 463−467.

(4) Hartstein, K. H.; Schimpf, A. M.; Salvador, M.; Gamelin, D. R. Cyclotron splittings in the plasmon resonances of electronically doped semiconductor nanocrystals probed by magnetic circular dichroism spectroscopy. *J. Phys. Chem. Lett.* **2017**, *8*, 1831−1836.

(5) Buonsanti, R.; Llordes, A.; Aloni, S.; Helms, B. A.; Milliron, D. J. Tunable infrared absorption and visible transparency of colloidal aluminum-doped zinc oxide nanocrystals. *Nano Lett.* **2011**, *11*, 4706−4710.

(6) Garcia, G.; Buonsanti, R.; Runnerstrom, E. L.; Mendelsberg, R. J.; Llordes, A.; Anders, A.; Richardson, T. J.; Milliron, D. J. Dynamically modulating the surface plasmon resonance of doped semiconductor nanocrystals. *Nano Lett.* **2011**, *11*, 4415−4420.

(7) Crockett, B. M.; Jansons, A. W.; Koskela, K. M.; Johnson, D. W.; Hutchison, J. E. Radial dopant placement for tuning plasmonic properties in metal oxide nanocrystals. *ACS Nano* **2017**, *11*, 7719−7728.

(8) Jansons, A. W.; Hutchison, J. E. Continuous growth of metal oxide nanocrystals: Enhanced control of nanocrystal size and radial dopant distribution. *ACS Nano* **2016**, *10*, 6942−6951.

(9) Mehra, S.; Bergerud, A.; Milliron, D. J.; Chan, E. M.; Salleo, A. Core/shell approach to dopant incorporation and shape control in colloidal zinc oxide nanorods. *Chem. Mater.* **2016**, *28*, 3454−3461.

(10) Quinn, S. D.; Rafferty, A.; Dick, E.; Morten, M. J.; Kettles, F. J.; Knox, C.; Murrie, M.; Magennis, S. W. Surface charge control of quantum dot blinking. *J. Phys. Chem. C* **2016**, *120*, 19487−19491.

(11) Zeng, Y.; Kelley, D. F. Surface charging in CdSe quantum dots: Infrared and transient absorption spectroscopy. *J. Phys. Chem. C* **2017**, *121*, 16657−16664.

(12) Krauss, T. D.; Brus, L. E. Charge, polarizability, and photoionization of single semiconductor nanocrystals. *Phys. Rev. Lett.* **1999**, *83*, 4840−4843.

(13) Krauss, T. D.; Brus, L. E. Erratum: Charge, polarizability, and photoionization of single semiconductor nanocrystals [Phys. Rev. Lett. 83, 4840 (1999)]. *Phys. Rev. Lett.* **2000**, *84*, 1638.

(14) Li, S.; Steigerwald, M. L.; Brus, L. E. Surface states in the photoionization of high-quality cdse core/shell nanocrystals. *ACS Nano* **2009**, *3*, 1267−1273.

(15) Yalcin, S. E.; Yang, B.; Labastide, J. A.; Barnes, M. D. Electrostatic force microscopy and spectral studies of electron attachment to single quantum dots on indium tin oxide substrates. *J. Phys. Chem. C* **2012**, *116*, 15847−15853.

(16) Costi, R.; Cohen, G.; Salant, A.; Rabani, E.; Banin, U. Electrostatic Force Microscopy Study of Single Au−CdSe Hybrid Nanodumbbells: Evidence for Light-Induced Charge Separation. *Nano Lett.* **2009**, *9*, 2031−2039.

(17) Jana, N. R.; Chen, Y.; Peng, X. Size- and shape-controlled magnetic (Cr, Mn, Fe, Co, Ni) oxide nanocrystals via a simple and general approach. *Chem. Mater.* **2004**, *16*, 3931−3935.

(18) Liang, X.; Ren, Y.; Bai, S.; Zhang, N.; Dai, X.; Wang, X.; He, H.; Jin, C.; Ye, Z.; Chen, Q.; et al. Colloidal indium-doped zinc oxide nanocrystals with tunable work function: Rational synthesis and optoelectronic applications. *Chem. Mater.* **2014**, *26*, 5169−5178.

(19) Lutterotti, L. Total pattern fitting for the combined size-strain-stress-texture determination in thin film diffraction. *Nucl. Instrum. Methods Phys. Res., Sect. B* **2010**, *268*, 334−340.

(20) Coffey, D. C.; Ginger, D. S. Time-resolved electrostatic force microscopy of polymer solar cells. *Nat. Mater.* **2006**, *5*, 735−740.

(21) Cox, P. A.; Glaz, M. S.; Harrison, J. S.; Peurifoy, S. R.; Coffey, D. C.; Ginger, D. S. Imaging charge transfer state excitations in polymer/fullerene solar cells with time-resolved electrostatic force microscopy. *J. Phys. Chem. Lett.* **2015**, *6*, 2852−2858.

(22) Giridharagopal, R.; Cox, P. A.; Ginger, D. S. Functional scanning probe imaging of nanostructured solar energy materials. *Acc. Chem. Res.* **2016**, *49*, 1769−1776.

(23) Chen, Y.; Kim, M.; Lian, G.; Johnson, M. B.; Peng, X. Side reactions in controlling the quality, yield, and stability of high quality colloidal nanocrystals. *J. Am. Chem. Soc.* **2005**, *127*, 13331−13337.

(24) Senger, R. T.; Bajaj, K. K. Optical properties of confined polaronic excitons in spherical ionic quantum dots. *Phys. Rev. B: Condens. Matter Mater. Phys.* **2003**, *68*, 045313.

(25) Ito, D.; Yokoyama, S.; Zaikova, T.; Masuko, K.; Hutchison, J. E. Synthesis of ligand-stabilized metal oxide nanocrystals and epitaxial core/shell nanocrystals via a lower-temperature esterification process. *ACS Nano* **2014**, *8*, 64−75.

(26) Singhal, A.; Achary, S. N.; Manjanna, J.; Chatterjee, S.; Ayyub, P.; Tyagi, A. K. Chemical synthesis and structural and magnetic

DOI: 10.1021/acs.jpcc.8b04718
J. Phys. Chem. C 2018, 122, 18596−18602

properties of dispersible cobalt- and nickel-doped ZnO nanocrystals. *J. Phys. Chem. C* **2010**, *114*, 3422−3430.
(27) Mendelsberg, R. J.; Garcia, G.; Li, H.; Manna, L.; Milliron, D. J. Understanding the plasmon resonance in ensembles of degenerately doped semiconductor nanocrystals. *J. Phys. Chem. C* **2012**, *116*, 12226−12231.
(28) Lounis, S. D.; Runnerstrom, E. L.; Llordés, A.; Milliron, D. J. Defect chemistry and plasmon physics of colloidal metal oxide nanocrystals. *J. Phys. Chem. Lett.* **2014**, *5*, 1564−1574.
(29) Della Gaspera, E.; Chesman, A. S. R.; van Embden, J.; Jasieniak, J. J. Non-injection synthesis of doped zinc oxide plasmonic nanocrystals. *ACS Nano* **2014**, *8*, 9154−9163.
(30) Hofman, E.; Robinson, R. J.; Li, Z.-J.; Dzikovski, B.; Zheng, W. Controlled dopant migration in CdS/ZnS core/shell quantum dots. *J. Am. Chem. Soc.* **2017**, *139*, 8878−8885.
(31) Norberg, N. S.; Parks, G. L.; Salley, G. M.; Gamelin, D. R. Giant Excitonic Zeeman Splittings in Colloidal Co^{2+}-Doped ZnSe Quantum Dots. *J. Am. Chem. Soc.* **2006**, *128*, 13195−13203.
(32) Schwartz, D. A.; Norberg, N. S.; Nguyen, Q. P.; Parker, J. M.; Gamelin, D. R. Magnetic Quantum Dots: Synthesis, Spectroscopy, and Magnetism of Co^{2+}- and Ni^{2+}-Doped ZnO Nanocrystals. *J. Am. Chem. Soc.* **2003**, *125*, 13205−13218.
(33) Zhou, D.; Kittilstved, K. R. Control over Fe^{3+} speciation in colloidal ZnO nanocrystals. *J. Mater. Chem. C* **2015**, *3*, 4352−4358.
(34) Wyckoff, R. W. G. Würtzite ZnO (zincite). *Crystal Structures*, 2nd ed.; Interscience Publishers: New York, 1963.
(35) Shannon, R. D. Revised effective ionic radii and systematic studies of interatomic distances in halides and chalcogenides. *Acta Crystallogr., Sect. A: Cryst. Phys., Diffr., Theor. Gen. Crystallogr.* **1976**, *32*, 751−767.
(36) Bendix, P. M.; Pedersen, L. J.; Nørregaard, K.; Oddershede, L. B. Optical trapping of nanoparticles and quantum dots. *IEEE J. Sel. Top. Quantum Electron.* **2014**, *20*, 15−26.
(37) Johnson, P. B.; Christy, R. W. Optical constants of the noble metals. *Phys. Rev. B: Solid State* **1972**, *6*, 4370−4379.

DOI: 10.1021/acs.jpcc.8b04718
J. Phys. Chem. C 2018, 122, 18596−18602